Research Article / *Araştırma Makalesi*

Ege Journal of Medicine / *Ege Tıp Dergisi* 2021; 61 (1): 22-29

# Computational investigation of fitting for calculation of signal dynamics from hyperpolarized xenon-129 Gas MRI

## *Hiperpolarize ksenon-129 Gaz MRG'den elde edilen sinyal dinamiğinin hesaplanması için uyarlamanın hesapsal incelenmesi*

Özkan Doğanay

Department of Basic Oncology, Health Science Institute, Ege University, Izmir, Turkiye

**ABSTRACT**

**Aim:** Computational fitting methods were investigated to determine the most accurate fitting approach for the calculation of dynamic hyperpolarized MRI parameters.

**Materials and Methods:** The signal decay of a time-series Hyperpolarized xenon gas MRI phantom was fitted to Bloch equations using three methods varying the fitting parameters for calculation of flip angle, α, and longitudinal relaxation time, $T_1$. The first fitting method used an initial calculation of α before the fitting process. The second and third techniques used direct fitting of signal decay equations with and without upper-lower boundaries for calculation of α, and $T_1$. Wilcoxon signed-rank test was used to investigate the statistical significance of the calculated parameters.

**Results:** The first approach was the most accurate fitting technique that allowed direct calculation of α=8.65° in agreement to the third approach α=8.73±0.78°, 8.75±0.12°, 8.67±0.05°. Additionally, the standard deviation of the calculated $T_1$ was lower than 1% ($T_1$=103.2±0.04s) which was significantly more accurate than the second method ($T_1$=90±30.2s and 135.7±10.3s) and the third method ($T_1$=101.4±5.1s and 113.5±16.1s).

**Conclusion:** The first technique provides repeatable and reliable calculation of signal decay parameters including α and $T_1$ from the dynamic hyperpolarized gas MR images and more accurate than direct fitting methods.

**Keywords:** Hyperpolarized MRI, Xenon-129, flip angle, longitudinal relaxation time, dynamic MRI.

***ÖZ***

***Amaç:*** *Dinamik hiperpolarize MRI parametrelerinin hesaplanmasında en doğru uyarlama yaklaşımını belirlemek için hesaplamalı uydurma yöntemleri araştırılmıştır.*

***Gereç ve Yöntem:*** *Bir zaman-serisi Hiperpolarize ksenon gazı MRG fantomunun sinyal bozunması, döndürme açısı α ve boylamsal azalma süresi T1'in hesaplanması için uyarlama parametrelerini değiştiren üç yöntem kullanılarak Bloch denklemlerine yerleştirilmiştir. İlk uyarlama yöntemi, uyarlama işleminden önce ilk α hesaplamasını kullanmaktadır. İkinci ve üçüncü teknikler α ve T1'in hesaplanması için üst ve alt limitleri olan ve olmayan sinyal bozunma denklemlerinin doğrudan uyarlamasını kullanmaktadır. Hesaplanan parametrelerin istatistiksel anlamlılığını araştırmak için Wilcoxon işaretli sıra testi kullanılmıştır.*

***Bulgular:*** *İlk yaklaşım, α = 8,65°'nin doğrudan hesaplanmasına izin veren en doğru uygulama tekniğidir ve üçüncü yaklaşımla uyumludur. Ek olarak, hesaplanan T1'in standart sapması %1'den düşüktür (T1 = 103,2 ± 0,04s) ve bu ikinci yöntem ile (T1 = 90 ± 30,2s ve 135,7 ± 10,3s) ve üçüncü yöntemden (T1 = 101,4 ± 5,1s ve 113,5 ± 16,1s) anlamlı derecede daha doğrudur.*

***Sonuç:*** *İlk teknik, dinamik hiperpolarize gaz MR görüntülerinden α ve T1 dâhil olmak üzere sinyal bozunma parametrelerinin tekrarlanabilir ve güvenilir bir şekilde hesaplanmasını ve doğrudan uyarlama yöntemlerinden daha doğru olmasını sağlamaktadır.*

***Anahtar Sözcükler:*** *Hiperpolarize MRG, ksenon-129, döndürme açısı, boylamsal azalma süresi, dinamik MRG.*

Corresponding author: Özkan Doğanay
Department of Basic Oncology, Health Science Institute, Ege University, Izmir, Turkiye
E-mail: *ozkandoganay@gmail.com*
Application date: 27.04.2021 Accepted: 19.08.2021

## INTRODUCTION

Hyperpolarized Xenon-129 gas Magnetic Resonance Imaging (MRI) is a growing field of interest for imaging of gas ventilation in the lungs and evaluating airway obstructions due to pulmonary diseases such as chronic obstructive pulmonary disease (COPD) (1-3), asthma (4-6) and idiopathic pulmonary fibrosis (7, 8) and gas-exchange between the alveolar airspace and veins (9-13). Nevertheless, the development of functional imaging and post-image processing strategies are necessary steps for implementing hyperpolarized gas MRI in the clinical routine. Functional MR imaging techniques were investigated widely regarding the development of k-space sampling trajectories for estimation of intrinsic flip angle variations, longitudinal and transverse decay of polarization due to the partial pressure of oxygen (14-20). However, without using optimized post-image processing techniques, estimated image parameters and clinical information derived from hyperpolarized MR images would be substantially wrong (21, 22). In this study, we investigated (i) how computational fitting techniques can lead to substantial deviations of the calculated MR parameters, and (i) how to reduce the large errors in hyperpolarized MR images.

Although terminology of the longitudinal relaxation time, $T_1$, has been used to be the same for both conventional MR imaging and hyperpolarized MRI, the actual meaning is different changing the interpretation and analysis of MR images (10, 23). While signal intensity increasing with $T_1$ in conventional MR due to the recovery of thermal polarization during the repetition time (TR) contributing to increased image contrast, the hyperpolarized MRI signal is not renewable and decays continuously from the hyperpolarization stage in two steps independent of TR: (i) during and after polarization process before the polarized gas is inhaled (24-27) and (ii) even more drastically decays when inhaled to the lungs due to presence of Oxygen during the actual MR scan (10, 19, 28). This continuous decay might be considered as a problem with hyperpolarized MRI, however, it presents a significant advantage for rapid signal acquisition that does not require a TR recovery in contrast to the thermal polarization (i.e. conventional MRI) (10, 29). Therefore, the optimum use of the strong hyperpolarized MR signal benefits using dedicated image acquisition strategies including the rapid k-space sampling, and fewer RF pulses (14, 30-34).

The hyperpolarized signal decay models and time-series image acquisition strategies have been shown to provide quantitative maps of flip angle variations based on the assumptions of no-inflow of gas into the signal decay region and immobility of the imaged subject (18, 19). Despite the data acquisition aspects and related deviations in the measured flip angle and longitudinal relaxation times were discussed in detail corroborating to signal decay equations, deviations in the calculated flip angle and $T_1$ due to the complexity of computational data fitting steps could cause errors in the calculated flip angle and $T_1$ (21).

In this work, the accuracy of the calculated flip angle and $T_1$ for hyperpolarized gas MRI were investigated corroborating the signal decay equations. In particular, the errors in the calculated fitting parameters were evaluated using three different fitting approaches thereby the best fitting approach with the least error estimation was determined for simultaneous calculation of hyperpolarized gas MR signal decay parameters including flip angle and $T_1$.

## MATERIALS and METHODS

**Signal decay:** As previously described (23, 35, 36), the hyperpolarized signal from dynamic ventilation MR images as a function of flip angle and the number of RF pulses is given by:

$$S = M_i\, e^{(-t/T_1)} \cos(\alpha)^{n-1} \sin(\alpha) \qquad [1]$$

where $M_i$ is a scaling factor that is dependent on the degree of hyperpolarization, amount of hyperpolarized gas and coil sensitivity, digital filter and amplifier; $T_1$ is the longitudinal relaxation time; α is the flip angle that excites gas magnetization in the hyperpolarized stage, n is the number of RF pulses.

Equation 1 describes the continuous decay of hyperpolarization signal from its initial value (i.e. $M_i$) and resulting decrease in image intensity as a function of T1, n, and α in contrast to the thermal polarization that replenishes every TR. For a dynamic image acquisition strategy, images were acquired sequentially where image intensity, S, decreases as a function of the number of RF pulses, n, in a closed system assuming that there is not any gas flow and motion throughout the imaging process. According to Eq. 1, the signal decay of a hyperpolarized time-series MRI from a gas phantom is shown in Figure-1 that was previously reported by Doganay et al (32).

**Initial flip angle calculation**: Conceptually, the relationship between the flip angle and signal decay can be modeled simply with Eq. 1 in free induction decay (FID) acquisitions, however, for the case of imaging, the image intensity weighted by the combination of multi-RF pulses and combination of each k-space readout data. In particular, the image intensity for the two-interleave spiral k-space sampling, which uses two RF pulses for each image acquisition and reconstruction, can be approximated by the multiplication of signal from each k-space. Thus, the ratio of first to second images can be written:

$$\frac{Image\ 1}{Image\ 2} \approx \frac{S(n=1)\times S(n=2)}{S(n=3)\times S(n=4)} = \frac{1}{\cos(\alpha)^4} \quad [2]$$

Hence, knowing the image intensities for Image 1 (t=0.5s) and Image 2 (t=1s) in Figure-1, the flip angle can be calculated as follows:

$$\alpha = \arccos\left(\sqrt[4]{\frac{Image\ 2}{Image\ 1}}\right) \quad [3]$$

Despite α can be calculated directly from Eq. 3, $M_i$ and $T_1$ can only be calculated fitting the signal decay data to Eq. 1.

**Fitting-first technique:** Two fitting parameters including $M_i$ and $T_1$ were calculated by fitting Eq. 1 to hyperpolarized signal decay data. To do so, the predefined nonlinear curve fitting function in MATLAB (lsqcurvefit, Matlab) was used knowing α from Eq. 3 and setting some initial guess values for $M_i$ and $T_1$ as summarized in Table-1. To investigate the effect of initial guess values on the calculation of $M_i$ and $T_1$, 20 different initial guess values were simulated as also shown in Table-1.

**Fitting-second technique:** All three fitting parameters including α, $M_i$, and $T_1$ were simultaneously calculated using the nonlinear curve fitting function without using the initial calculation of α in Eq. 3. An approximate estimate of the error caused by the choice of initial guess values was made by varying the initial guess values as summarized in Table-2.

**Fitting-third technique:** The influence of lower and upper boundary conditions on the calculation of α, $M_i$, and $T_1$ was investigated using upper and lower bounds as same as the initial guess values: i) $M_i$ from $1\times10^4$ A.U. to $1\times10^6$ A.U., ii) $T_1$ from 60 s to 120 s, and iii) α from 1° to 20°, the calculated fitting parameters: α, $M_i$ and $T_1$ were simulated as summarized in Table-3. Wilcoxon signed-rank test (GraphPad Software, La Jolla California USA) was then used to investigate statistical differences in the calculated α and $T_1$ between the three methods.

## RESULTS

**First technique:** Figure-1 shows the signal decay of a time-series MRI xenon gas phantom. Flip angle was calculated to be α = 8.65° from Eq. 3 using Images 1 and 2 in Figure-1 without using the fitting technique. Then, knowing α, the other two signal decay parameters in Eq. 1 including $M_i$, and $T_1$ were calculated to be 107443 A.U. and 103.2 s using the initial guess values $M_i = 1\times10^5$ A.U. and $T_1$=100 s. Figure-2 (a) shows the signal decay data points from the time-series images for a chosen ROI as shown in Figure-1 including the corresponding fitting curve. To investigate the influence of initial guess values, Figure-2 (b-c) shows how $T_1$ and $M_i$ calculations varied as a function of the initial guess values, respectively. The calculated mean $T_1$ values were 103.3±0.04 s and 103.3±0.08 s for the corresponding initial guess values as summarized in Table-1 and statistically not different (p=0.069).

**Second technique:** The calculated α, $T_1$, and $M_i$ values using directly fitting of Eq. 1 to signal decay data were summarized in Table-2 using the initial guess values. Particularly, calculated α = 9.4° using this fitting method was approximately 10% greater than the direct calculation of α = 8.65° in Table-1. In a close inspection, the variations of $T_1$ as a function of initial guess values of α, $T_1$, and $M_i$ are shown in Figure-3 (a-c), respectively. The mean of calculated $T_1$ values varied from 135.7±10.3 s to 90±30.2 s as also summarized in Table-2 depending on the initial guess values as well as the average flip angles varied between 8.48±0.48° and 9.48±0.03°. The calculated $T_1$ and α in Table 2 were statistically significantly different than Table-1 (p<0.001).

**Third technique:** Fitting was performed using the upper and lower bounds for $M_i$ from $1\times10^4$ A.U. to $1\times10^6$ A.U., $T_1$ from 60 s to 120 s, and α from 5° to 15°. The calculated fitting parameters were summarized in Table-3 and approached to the proposed technique in Table-1 when upper and lower bounds values were included in the fitting process that used the same initial guess values in Table-2. The variations of fitting parameters are also shown in Figure-4 (a-c). The lower and upper bounds provided a more accurate calculation of fitting parameters than those of calculated fitting parameters in Table-2. Additionally, the calculated $T_1$ was statistically not different than those of Table-1 with p=0.06 and different than those in Table-2 with p<0.0001 respectively.

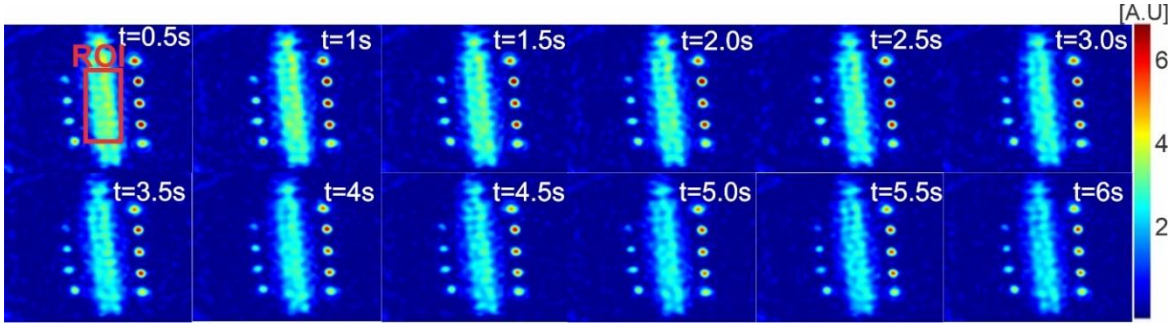


**Figure-1.** Signal decay of a gas phantom is shown for a time-series MR image acquisition from 0 s to 6 s. ROI is the region of interest for obtaining the signal decay data. Colour bar represents the intensity of hyperpolarized Xenon-129 signal associated to the term Mi in Eq 1 (Figure reproduced with permission from Doganay et al [32]).

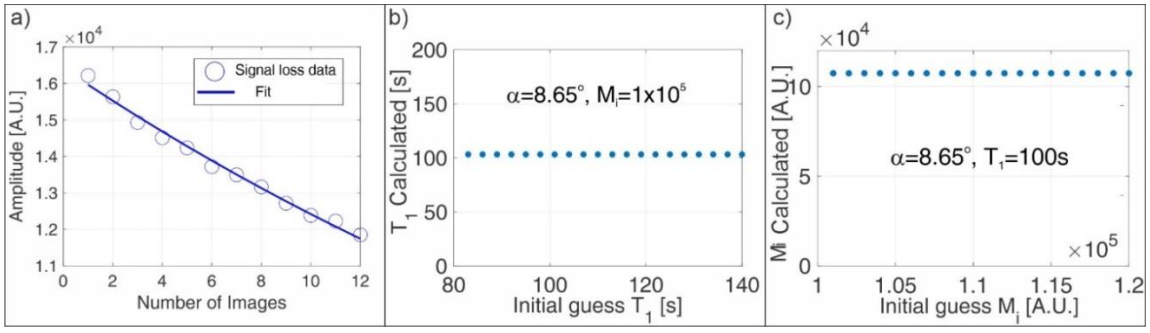


**Figure-2.** Signal decay from the time-series images and the corresponding fitting from Eq. 1 is shown in (a) with data points and solid line, respectively. Calculated $T_1$ as a function of initial guess $T_1$ values are shown in (b) and Measured Mi as a function of initial guess Mi are shown in (c).

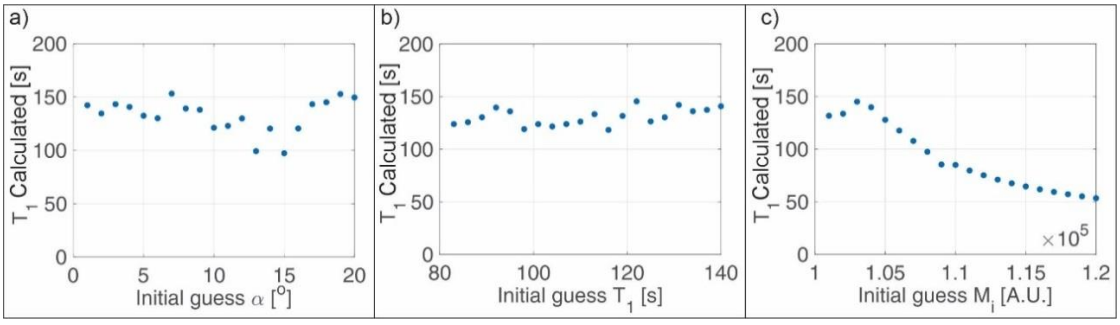


**Figure-3.** The effects of initial guess values for α, $T_1$, and $M_i$ on the measured $T_1$ are shown respectively in (a), (b), and (c).

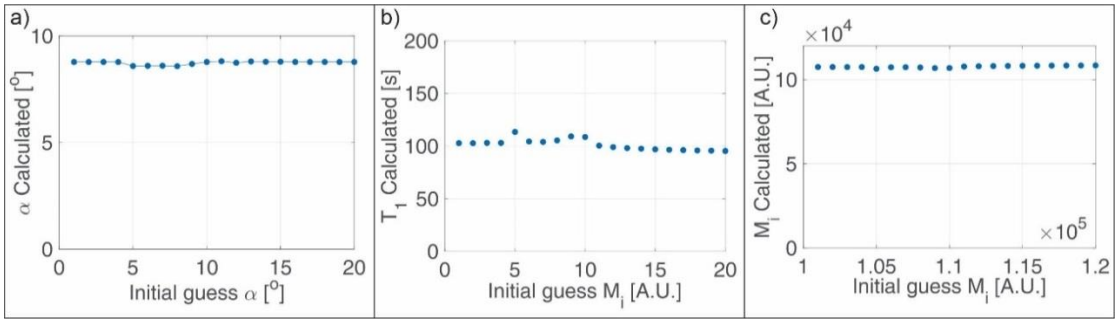


**Figure-4.** The variations of calculated α, $T_1$, and $M_i$ depending on initial guess values are shown in (a-c) respectively.

**Table-1** Fitting parameters calculated using the first technique.

| | Calculated using Eq. 1 | | | | Initial guess values | | Eq. 3 |
|---|---|---|---|---|---|---|---|
| | $M_i$ [A.U.] | | $T_1$ [s] | | $M_i$ [A.U.] | $T_1$ [s] | α [°] |
| **Constant Initial guess** | 107443 | | 103.2 | | $1\times10^5$ | 100 | 8.65 |
| | Mean | Std | Mean | Std | | | |
| **Varying $T_1$ initial guess** | 107443 | 0.1 | 103.2 | 0.04 | $1\times10^5$ | **60-120** | |
| **Varying $M_i$ initial guess** | 107443 | 0.1 | 103.2 | 0.08 | **$1\times10^5$-$1.2\times10^5$** | 100 | |

**Table-2.** Fitting parameters calculated using the second technique.

| | Calculated using Eq. 1 | | | | | | Initial guess values | | |
|---|---|---|---|---|---|---|---|---|---|
| | $M_i$ [A.U.] | | $T_1$ [s] | | α [°] | | $M_i$ [A.U.] | $T_1$ [s] | α [°] |
| **Constant initial guess** | 100145 | | 138 | | 9.4 | | $1\times10^5$ | 100 | 9 |
| | Mean | Std | Mean | Std | Mean | Std | | | |
| **Varying α initial guess** | 99977 | 138 | 130.2 | 18.8 | 9.48 | 0.03 | $1\times10^5$ | 100 | **1-20** |
| **Varying $T_1$ initial guess** | 99962 | 180 | 135.7 | 10.3 | 9.47 | 0.03 | $1\times10^5$ | **60-120** | 9 |
| **Varying $M_i$ initial guess** | 110541 | 5914 | 90 | 30.2 | 8.48 | 0.48 | **$1\times10^5$-$1.2\times10^5$** | 100 | 9 |

**Table-3.** Fitting parameters calculated using the third technique.

| | Calculated using Eq. 1 | | | | | | Initial guess values | | |
|---|---|---|---|---|---|---|---|---|---|
| | $M_i$ [A.U.] | | $T_1$ [s] | | α [°] | | $M_i$ [A.U.] | $T_1$ [s] | α [°] |
| **Constant initial guess** | 107650 | | 101.2 | | 8.67 | | $1\times10^5$ | 100 | 9 |
| | Mean | Std | Mean | Std | Mean | Std | | | |
| **Varying α initial guess** | 106842 | 987 | 109.9 | 9.1 | 8.73 | 0.78 | $1\times10^5$ | 100 | **1-20** |
| **Varying $T_1$ initial guess** | 106662 | 1505 | 113.5 | 16.1 | 8.75 | 0.12 | $1\times10^5$ | **60-120** | 9 |
| **Varying $M_i$ initial guess** | 107686 | 575 | 101.4 | 5.1 | 8.67 | 0.05 | **$1\times10^5$-$1.2\times10^5$** | 100 | 9 |

## DISCUSSION

In this work, three fitting methods were investigated to calculate signal decay parameters of time-series hyperpolarized MR images including, $M_i$, α, and $T_1$, and to determine the discrepancy between the calculated parameters. Using the initial calculated flip angle with the first method, $M_i$ and $T_1$ were more accurately calculated with a very low standard deviation that is less than 1% of the mean value in Table-1 in comparison to the other two approaches in Table-2-3. Additionally, the first method allowed a more independent calculation of the fitting parameters providing a more straightforward and practical method without using upper and lower bounds. The first technique provides a more robust and practical way of calculating fitting parameters than second and third techniques.

In the past, several hyperpolarized gas MRI studies implemented a least-squares linear fitting method that is similar to the second technique in this study (21, 22, 28, 35), however, the source of error in the calculated signal decay parameters due to the fitting related computational discrepancies has not been investigated quantitatively. The proposed first technique in this study indicates that it is feasible to calculate $M_i$, α, and $T_1$ within a standard deviation of less than 1% which is significantly better than second and third techniques when the same boundary conditions (i.e. initial guess values) were used. The qualitative and consistent agreement between mean $M_i$ and $T_1$ values in Table-1 while changing the initial guess values suggested that the initial-calculated flip angle significantly reduces the deviations in the calculated $M_i$ and $T_1$ with the first technique in comparison to the second technique where $M_i$, α, and $T_1$ were calculated simultaneously in Table-2. The initial

guess values were selected to be the same for a fair comparison between three techniques. While the calculated mean α values varied approximately 10% in Table-2 with the second technique, the calculated $T_1$ values were varied more significantly between 90±30.2 and 135.7±10.3 s suggesting that direct fitting of Eq. 1 to signal decay data is affected by changing the initial guess values and is not reliable solely for the simultaneous measurement of $M_i$, α, and $T_1$. In contrast to the direct fitting (i.e. the second technique), the proposed first technique showed that the calculated mean $T_1$ was the same and the standard deviations were less than 1% of the mean values suggesting that fitting error was negligible for the same boundary conditions. Although previous studies reported variations in the calculated parameters may be caused by fitting errors, the influence of fitting errors was not determined specifically (21). Our findings indicate that the calculated fitting parameters can vary up to 50% depending on the fitting method as also illustrated by Figure-3. The investigators then better use the first method for extracting the fitting parameters and for eliminating fitting-related errors not only for hyperpolarized gas MR but also other hyperpolarized MR studies including Carbon-13.

Unlike the second technique (Table-2), the third method that incorporates additional information of upper-lower bounds in the fitting process (Table-3), mean $M_i$, α, and $T_1$ values were approached more to the calculated fitting parameters in Table-1. The same initial guess value range did not affect the calculated fitting parameters. For instance, α = 8.65° calculated directly from Eq. 3 was not statistically different than the calculated flip angles: 8.73±0.78°, 8.75±0.12°, 8.67±0.05° with $p<0.001$. Since there is not any available technique for absolute measurement of flip angle, the repeatability of the calculated flip angles using two different approaches confirms the fitting accuracy.

Nonetheless, the mean and standard deviations of the calculated fitting parameters vary less with the use of upper-lower bounds and approach to the calculated values with the proposed method, the proposed method is more repeatable reducing the complexity of fitting and the standard deviations of the calculated values only vary less than 1% over the mean providing a substantial improvement in the estimation of fitting parameters independent of experimental conditions. Accordingly, the fitting approach with the initial calculation of flip angle provided the most accurate calculation of fitting parameters.

In this study, we used phantom MR images for investigating the computational limits related to the fitting errors and techniques and for determining the best fitting approach. The calculated $T_1$ was in the order of 103.2±0.04 s due to low oxygen concentration in the phantom which is in the order of 10-15s in lungs as previously reported (10, 21, 22, 37). In the future, the proposed technique will focus on the implementation of this technique to human lung imaging and the investigation of oxygen partial pressure variations. Although the flip angle can be prescribed before the actual MR scan, the prescribed and actual flip angles can vary significantly depending on the RF coil coupling and intrinsic transmit in homogeneities of the RF hardware may resulting in artificial ventilation image heterogeneities (38). This technique does not require any pre-existing knowledge of scan parameters for calculation of α and $T_1$ and allows correction of artificial image variations in time-series (i.e. sequential) hyperpolarized MR images that recently gain interest for dynamic imaging of lung ventilation and gas exchange.

## CONCLUSION

Post image processing of hyperpolarized gas time-series MR images with the proposed technique in this study, allow the calculation of α and $T_1$ with a standard deviation of less than 1%. While demonstrated in this study, T1 can also be calculated with high repeatability independent of fitting errors using the initial calculation of flip angle allowing reduction of the standard deviation of the calculated fitting parameters of approximately 50%. More practically, this technique does eliminate the use of any assumption for the calculation of α and $T_1$ and the effects of fitting boundary conditions (i.e. initial guess values).

**Funding:** This study was funded by TUBİTAK (Program 2232, grant number: 118C189).

**Conflict of Interest:** The author declares that he has no conflict of interest.

**Ethical approval:** This article does not contain any studies with human participants or animals performed by any of the authors.

**References**


1. Matin TN, Rahman N, Nickol AH, et al. Chronic Obstructive Pulmonary Disease: Lobar Analysis with Hyperpolarized 129Xe MR Imaging. Radiology. 2017; 282: 857-68.
2. Chen M, Doganay O, Matin T, et al. Delayed ventilation assessment using fast dynamic hyperpolarised Xenon-129 magnetic resonance imaging. Eur Radiol. 2019.
3. Qing K, Tustison NJ, Mugler JP, 3rd, et al. Probing Changes in Lung Physiology in COPD Using CT, Perfusion MRI, and Hyperpolarized Xenon-129 MRI. Acad Radiol. 2019; 26: 326-34.
4. He M, Driehuys B, Que LG, Huang YT. Using Hyperpolarized 129Xe MRI to Quantify the Pulmonary Ventilation Distribution. Acad Radiol. 2016; 23: 1521-31.
5. Svenningsen S, Guo F, Kirby M, et al. Pulmonary functional magnetic resonance imaging: asthma temporal-spatial maps. Acad Radiol. 2014; 21: 1402-10.
6. Shukla Y, Wheatley A, Kirby M, et al. Hyperpolarized 129Xe magnetic resonance imaging: tolerability in healthy volunteers and subjects with pulmonary disease. Acad Radiol. 2012; 19: 941-51.
7. Wild JM. Imaging pathophysiological changes in the lungs in IPF with xenon magnetic resonance imaging. Thorax. 2018; 73:1.
8. Mammarappallil JG, Rankine L, Wild JM, Driehuys B. New Developments in Imaging Idiopathic Pulmonary Fibrosis With Hyperpolarized Xenon Magnetic Resonance Imaging. J Thorac Imaging. 2019; 34: 136-50.
9. Doganay O, Chen M, Matin T, et al. Magnetic resonance imaging of the time course of hyperpolarized (129) Xe gas exchange in the human lungs and heart. Eur Radiol. 2019; 29: 2283-92.
10. Marshall H, Stewart NJ, Chan H-F, Rao M, Norquay G, Wild JM. In vivo methods and applications of xenon-129 magnetic resonance. Progress in Nuclear Magnetic Resonance Spectroscopy. 2021; 122: 42-62.
11. Kern AL, Gutberlet M, Voskrebenzev A, et al. Mapping of regional lung microstructural parameters using hyperpolarized (129) Xe dissolved-phase MRI in healthy volunteers and patients with chronic obstructive pulmonary disease. Magn Reson Med. 2019; 81:2360-73.
12. Ruppert K, Hamedani H, Amzajerdian F, et al. Assessment of Pulmonary Gas Transport in Rabbits Using Hyperpolarized Xenon-129 Magnetic Resonance Imaging. Scientific Reports. 2018; 8:7310.
13. Patz S, Muradyan I, Hrovat MI, et al. Diffusion of hyperpolarized Xe-129 in the lung: a simplified model of Xe-129 septal uptake and experimental results. New J Phys. 2011; 13.
14. Marshall H, Ajraoui S, Deppe MH, Parra-Robles J, Wild JM. K-space filter deconvolution and flip angle self-calibration in 2D radial hyperpolarised 3He lung MRI. NMR in biomedicine. 2012; 25:389-99.
15. Wild JM, Paley MN, Viallon M, Schreiber WG, van Beek EJ, Griffiths PD. k-space filtering in 2D gradient-echo breath-hold hyperpolarized 3He MRI: spatial resolution and signal-to-noise ratio considerations. Magn Reson Med. 2002; 47: 687-95.
16. Wild JM, Paley MN, Kasuboski L, et al. Dynamic radial projection MRI of inhaled hyperpolarized 3He gas. Magn Reson Med. 2003; 49: 991-7.
17. Xu X, Norquay G, Parnell SR, et al. Hyperpolarized 129Xe gas lung MRI-SNR and T2* comparisons at 1.5 T and 3 T. Magn Reson Med. 2012; 68: 1900-4.
18. Ajraoui S, Parra-Robles J, Marshall H, Deppe MH, Clemence M, Wild JM. Acquisition of (3) He ventilation images, ADC, T(2)* and B(1) maps in a single scan with compressed sensing. NMR in biomedicine. 2012; 25: 44-51.
19. Marshall H, Parra-Robles J, Deppe MH, Lipson DA, Lawson R, Wild JM. (3) He pO2 mapping is limited by delayed-ventilation and diffusion in chronic obstructive pulmonary disease. Magn Reson Med. 2014; 71:1172-8.
20. Ruppert K, Amzajerdian F, Hamedani H, et al. Assessment of flip angle-TR equivalence for standardized dissolved-phase imaging of the lung with hyperpolarized 129Xe MRI. Magn Reson Med. 2019; 81:1784-94.
21. Zhong J, Ruan W, Han Y, Sun X, Ye C, Zhou X. Fast Determination of Flip Angle and T1 in Hyperpolarized Gas MRI During a Single Breath-Hold. Sci Rep. 2016; 6: 25854.
22. Doganay O, Matin T, Chen M, et al. Time-series hyperpolarized xenon-129 MRI of lobar lung ventilation of COPD in comparison to V/Q-SPECT/CT and CT. Eur Radiol. 2019; 29: 4058-67.

23. Miller GW, Altes TA, Brookeman JR, De Lange EE, Mugler JP, 3rd. Hyperpolarized 3He lung ventilation imaging with B1-inhomogeneity correction in a single breath-hold scan. Magma. 2004; 16: 218-26.
24. Norquay G, Collier GJ, Rao M, Stewart NJ, Wild JM. ^{129}Xe-Rb Spin-Exchange Optical Pumping with High Photon Efficiency. Phys Rev Lett. 2018; 121:153201.
25. Nikolaou P, Coffey AM, Walkup LL, et al. XeNA: an automated 'open-source' (129)Xe hyperpolarizer for clinical use. Magnetic resonance imaging. 2014; 32:541-50.
26. Hersman FW, Ruset IC, Ketel S, et al. Large production system for hyperpolarized 129 Xe for human lung imaging studies. Acad Radiol. 2008; 15: 683-92.
27. Driehuys B, Pollaro J, Cofer GP. In vivo MRI using real-time production of hyperpolarized 129 Xe. Magn Reson Med. 2008; 60:14-20.
28. Wild JM, Fichele S, Woodhouse N, Paley MN, Kasuboski L, van Beek EJ. 3D volume-localized pO2 measurement in the human lung with 3He MRI. Magn Reson Med. 2005; 53: 1055-64.
29. Fain SB, Carey K, Barton GP, Sorkness RL. Basics and Clinical Application of the MR Assessment of Ventilation. In: Ohno Y, Hatabu H, Kauczor H-U, editors. Pulmonary Functional Imaging: Basics and Clinical Applications. Cham: Springer International Publishing; 2021. p. 59-89.
30. Xiao S, Deng H, Duan C, et al. Considering low-rank, sparse and gas-inflow effects constraints for accelerated pulmonary dynamic hyperpolarized (129) Xe MRI. Journal of magnetic resonance. 2018; 290:29-37.
31. Xiao S, Deng H, Duan C, et al. Highly and Adaptively Undersampling Pattern for Pulmonary Hyperpolarized 129Xe Dynamic MRI. IEEE transactions on medical imaging. 2018.
32. Doganay O, Matin TN, McIntyre A, et al. Fast dynamic ventilation MRI of hyperpolarized (129) Xe using spiral imaging. Magn Reson Med. 2018; 79: 2597-606.
33. Wiesinger F, Weidl E, Menzel MI, et al. IDEAL spiral CSI for dynamic metabolic MR imaging of hyperpolarized [1-13C]pyruvate. Magn Reson Med. 2012; 68:8-16.
34. Lau AZ, Chen AP, Ghugre NR, et al. Rapid multislice imaging of hyperpolarized 13C pyruvate and bicarbonate in the heart. Magn Reson Med. 2010; 64:1323-31.
35. Doganay O, Wade T, Hegarty E, McKenzie C, Schulte RF, Santyr GE. Hyperpolarized (129) Xe imaging of the rat lung using spiral IDEAL. Magn Reson Med. 2016; 76: 566-76.
36. Zhao L, Mulkern R, Tseng CH, et al. Gradient-Echo Imaging Considerations for Hyperpolarized 129Xe MR. J Magn Reson B. 1996; 113: 179-83.
37. Patz S, Hersman FW, Muradian I, et al. Hyperpolarized (129) Xe MRI: a viable functional lung imaging modality? Eur J Radiol. 2007; 64:335-44.
38. Doganay O, Thind K, Wade T, Ouriadov A, Santyr GE. Transmit-only/receive-only radiofrequency coil configuration for hyperpolarized129Xe MRI of rat lungs. Concepts in Magnetic Resonance Part B: Magnetic Resonance Engineering. 2015; 45: 115-24.